INTERNATIONAL JOURNAL FOR NUMERICAL METHODS IN FLUIDS
Int. J. Numer. Meth. Fluids 2008; **56**:723–738
Published online 19 June 2007 in Wiley InterScience (www.interscience.wiley.com). DOI: 10.1002/fld.1552

Simulation of flow around a thin, flexible obstruction by means of a deforming grid overlapping a fixed grid

Kunlun Liu, Hari Radhakrishnan and Victor H. Barocas*, †

Department of Biomedical Engineering, University of Minnesota, Minneapolis, MN 55455, U.S.A.

SUMMARY

This paper presents a numerical method for simulation of coupled flows, in which the fluid interacts with a thin deformable solid, such as flows in cardiovascular valves. The proposed method employs an arbitrary Lagrangian–Eulerian (ALE) method for flow near the solid, embodied in the outflow domain in which the mesh is fixed. The method was tested by modelling a two-dimensional channel flow with a neo-Hookean obstacle, an idealization of the coupled flow near a cardiovascular valve. The effects of the Reynolds number and the dimensionless elastic modulus of the material on the wall shear stress, the size of the downstream reverse flows, and the velocity and pressure profiles were investigated. The deformation of the obstacle, the pressure drop across the obstacle, and the size of the top reverse flow increased as the Reynolds number increased. Conversely, increasing the elastic modulus of the obstacle decreased the deformation of the obstacle and the size of the top reverse flows, but did not affect the pressure drop across the obstacle over the range studied. Copyright © 2007 John Wiley & Sons, Ltd.

Received 9 November 2006; Revised 30 April 2007; Accepted 14 May 2007

KEY WORDS: incompressible Navier–Stokes equations; fluid–solid interaction; domain decomposition; overlapping grid

1. INTRODUCTION

Fluid–structure interaction problems, also called coupled flow problems, are an extremely challenging and active area of research in computational fluid mechanics, including bio-fluid mechanics. The mechanical interaction between a deformable solid and a fluid presents a unique set of challenges during modelling because of the coupling between the two materials. The deformation of the solid cannot be determined without knowing the stresses from the fluid, and the flow field

*Correspondence to: Victor H. Barocas, 7-105 Hasselmo Hall, 312 Church St SE, Minneapolis, MN 55455, U.S.A.
†E-mail: baroc001@umn.edu

Contract/grant sponsor: National Institutes of Health; contract/grant number: 1R01 HL071538-01
Contract/grant sponsor: University of Minnesota Supercomputing Institute

of the fluid cannot be determined without knowing the position of the solid. The two physical problems must be solved simultaneously to obtain meaningful results. Coupled flow problems range from the very large length scale of aeroelasticity problems [1] to the very small length scale of microfluidics problems. Within biomechanics, examples of fluid–structure interaction include flows interacting with iris [2], vessel wall [3, 4], valve leaflet [5–8], and ventricular wall [9].

Because the fluid domain is not known *a priori*, computational models for coupled flows must include a mechanism to adjust the fluid domain to conform to the deforming solid. Two fundamental strategies exist for mesh-based methods: deforming-grid methods or fixed-grid methods.

In deforming-grid methods, the mesh fills the fluid domain and deforms in response to changes in the shape of fluid domain. A procedure is needed to account for the motion of the finite-element nodes as they move to conform to the changing domain shape. The most popular strategy is probably the so-called arbitrary Lagrangian–Eulerian (ALE) method [10–12] (also known as domain deformation or pseudo-solid), in which finite-element nodes move affinely with the deformation of a fictitious solid occupying the fluid domain. Thus, as the fluid domain deforms, the imaginary solid also deforms, and the finite-element mesh adjusts accordingly. The ALE approach is highly successful for relatively small domain deformations but for large domain deformations, the mesh can get distorted severely, which introduces numerical errors and requires a costly remesh [13].

A contrasting approach is the fixed-grid method, in which the fluid domain is artificially placed onto a fixed grid, usually a structured grid to allow use of more efficient linear solvers. The fluid–solid boundaries are not enforced explicitly as in the deforming-grid methods, but are instead imposed implicitly as a constraint on the flow field. Flow results outside the true physical domain are then discarded. The 'immersed boundary' method of Peskin [14], in which the solid is modelled as a series of point interactions governed by finite-difference interpolation rules, is a well known and popular example, having been used in various forms by others as well [14, 15]. Formal introduction of the constraint *via* a distributed Lagrange multiplier (DLM) has also been highly successful [16, 17]. The DLM approach has the advantage that the constraint is applied continuously rather than pointwise, and it can be incorporated naturally into a finite-element framework.

Coupled flows in cardiovascular valves present additional challenges for both approaches. The large displacement of the valve leads to large mesh deformation in a deforming-grid model, and requires multiple remeshes at prohibitive computational cost. In contrast, the fixed-grid approach does not require remeshing, but it is poorly suited to very thin structures, which produce large pressure drops over small distances. The pressure drop across the valve must be accommodated by a large pressure gradient in the fixed grid. Because the valve does not conform to the grid, the entire pressure drop must be generated within the grid elements that contain the valve. The steep gradient in a fluid problem is both physically and numerically unattractive. If the valve is thinner than a fixed grid element containing it, the large pressure gradient within one element may destabilize the calculation.

Baaijens and coworkers [18] have developed a series of DLM-based codes for valve mechanics, and they have recently developed a hybrid scheme [5] in which an otherwise fixed grid is remeshed in the vicinity of the deforming valve. The local remesh is considerably less expensive than a global remesh, and the problem of steep pressure gradients is eliminated because the valve does not cut any fixed-grid element. However, there are two major issues that are not addressed by this approach. First, the remesh, which changes the distribution of the elements, may not conserve mass globally because conservation of mass is enforced only in an elemental sense. Second, and perhaps more important in view of the overall goal of modelling extremely complex three-dimensional flows,

DOI: 10.1002/fld

the loss of structure associated with the remesh severely limits the potential to employ a high-performance structured-grid solver for the fixed grid.

Based on these observations, we conclude that a true fixed-grid approach is desirable for incorporating the effect of the solid on the flow field as a whole, but a deforming-grid approach is desirable in the region near the valve so as to conform to the valve geometry. The objective of this work was to develop and test such a scheme. To test the applicability of this scheme in modelling valvular haemodynamics, the mechanics of a coupled flow in a two-dimensional channel with a thin flexible neo-Hookean obstacle was investigated.

2. GOVERNING EQUATIONS AND DOMAIN DECOMPOSITION

2.1. Governing equations

The flow of a viscous, incompressible fluid around a submerged object (Figure 1) is represented by the Navier–Stokes equations. Conservation of momentum is given by

$$\rho_{\mathrm{F}}\left(\frac{\partial \mathbf{v}}{\partial t}+\mathbf{v}\cdot\nabla\mathbf{v}\right)-\nabla\cdot\mathbf{T}=\mathbf{0} \tag{1}$$

$$\mathbf{T}\equiv -pI+\mu(\nabla\mathbf{v}+\nabla\mathbf{v}^{\mathrm{T}}) \tag{2}$$

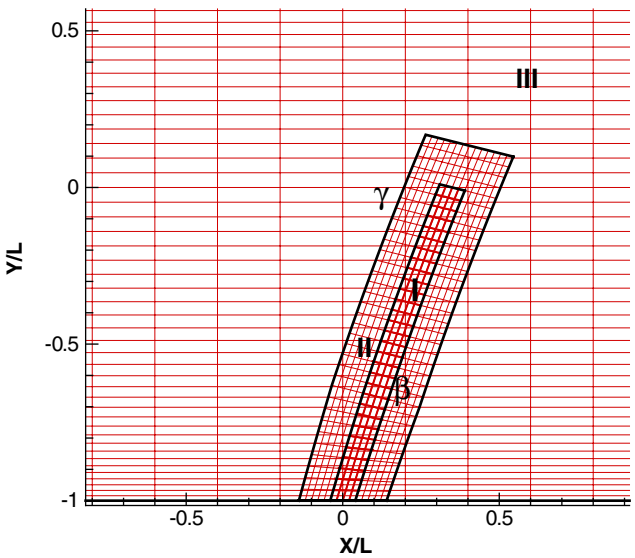

Figure 1. Configuration of the numerical domain used to model coupled two-dimensional channel flow. Part of the numerical region in the vicinity of the valve is shown. The regions I, II, and III correspond to the valve, inner fluid, and outer fluid regions. γ is the interface between the inner and outer regions where velocity and pressure matching is imposed implicitly, and β is the interface between the inner and valve regions where the no-slip boundary condition and continuity of stress in the liquid and solid are imposed explicitly.

DOI: 10.1002/fld

where $\mathbf{T}$ is the viscous stress in the fluid, p is the hydrostatic pressure, $\mathbf{v}$ is the fluid velocity, ρ_F is the fluid density, and μ is the fluid viscosity. Because the fluid is taken to be incompressible, conservation of mass is represented by the continuity equation:

$$\nabla \cdot \mathbf{v} = 0 \tag{3}$$

At the interface between the flow and the solid, the velocity of the solid and the velocity of the liquid are the same, i.e. there is no slip. Additionally, the stresses of the flow and solid must balance, that is

$$\mathbf{n}_F \cdot \mathbf{T} = \mathbf{n}_S \cdot \sigma \tag{4}$$

Here, σ is the Cauchy stress in the solid, and $\mathbf{n}_F$ and $\mathbf{n}_S$ are the normal to the surface of fluid and solid, respectively. The Cauchy stress σ depends on the constitutive nature of the material; in this work, the solid is modelled as neo-Hookean [19]:

$$\sigma = -\pi \mathbf{I} + E(\mathbf{F}\mathbf{F}^T) \tag{5}$$

where $\mathbf{F}$ is the deformation gradient given by $\mathbf{F} = \partial(\mathbf{x})/\partial\mathbf{X}$, where $\mathbf{x}$ is the deformed position of the solid and $\mathbf{X}$ is the undeformed position. The quantity π is the isotropic part of the elastic stress in the solid, equivalent to pressure in a fluid, and is given by

$$\pi = \frac{E}{1-2v} \ln(\det \mathbf{B}) \tag{6}$$

where $\mathbf{B}$ is the Finger tensor given by $\mathbf{B} = \mathbf{F}\mathbf{F}^T$. In this study, Poisson's ratio v is set as 0.491 for all the cases to represent a nearly incompressible material. The conservation of momentum for the solid is given by Cauchy's equation of stress:

$$\rho_S \frac{D^2\mathbf{x}}{Dt^2} - \nabla \cdot \sigma = \mathbf{0} \tag{7}$$

where ρ_S is the density of the solid. Notice that when the solid is nearly incompressible or the deformation is small, $\det \mathbf{B}$ is close to 1. In this circumstance, the Taylor expansion of $\ln(\det \mathbf{B})$ gives

$$\ln(\det \mathbf{B}) \approx \det \mathbf{B} - 1 \tag{8}$$

This implies that π in Equation (6) can be approximated by $(E/(1-2v))(\det \mathbf{B} - 1)$ provided that the dilatation of material is small. This substitution accelerates the numerical simulation considerably and was used when $|\det \mathbf{B} - 1| \leqslant 0.1$.

2.2. *The dimensionless governing equations*

The governing equations were nondimensionalized using the following reference coefficients:

$$\mathbf{v} = U_b \mathbf{v}^*, \quad \mathbf{X} = L\mathbf{X}^*, \quad \mathbf{x} = L\mathbf{x}^*, \quad t = \frac{L}{U_b} t^*, \quad p = \rho_F U_b^2 p^* \tag{9}$$

DOI: 10.1002/fld

Here U_b is the bulk velocity of the fluid, L is the length of the valve, and ρ_F is the density of the fluid. Thus, the dimensionless governing equation for the fluid reads

$$\frac{\partial \mathbf{v}^*}{\partial t^*} + \mathbf{v}^* \cdot \nabla \mathbf{v}^* + \nabla p^* - \frac{1}{Re} \nabla \cdot (\nabla \mathbf{v}^* + \nabla \mathbf{v}^{*\mathrm{T}}) = \mathbf{0} \tag{10}$$

$$\nabla \cdot \mathbf{v}^* = 0 \tag{11}$$

where Re is the Reynolds number. From Equations (5) and (7), the governing equation for the solid reduces to

$$\frac{\mathrm{D}^2 \mathbf{x}^*}{\mathrm{D}t^{*2}} - \tilde{E} \nabla \cdot \left[\mathbf{B}^* - \frac{\ln(\det \mathbf{B}^*)}{1 - 2v} \mathbf{I} \right] = \mathbf{0} \tag{12}$$

where ρ_S is the density of the solid and the dimensionless modulus $\tilde{E}$ is given by $E/\rho_S U_b^2$.

For the sake of convenience, the superscript * is dropped in the rest of this paper. The dimensionless governing equations are written as

$$\frac{\partial \mathbf{v}}{\partial t} + \mathbf{v} \cdot \nabla \mathbf{v} + \nabla p - \frac{1}{Re} \nabla \cdot (\nabla \mathbf{v} + \nabla \mathbf{v}^{\mathrm{T}}) = \mathbf{0} \tag{13}$$

$$\nabla \cdot \mathbf{v} = 0 \tag{14}$$

for the fluid and

$$\frac{\mathrm{D}^2 \mathbf{x}}{\mathrm{D}t^2} - \tilde{E} \nabla \cdot \left[\mathbf{B} - \frac{\ln(\det \mathbf{B})}{1 - 2v} \mathbf{I} \right] = \mathbf{0} \tag{15}$$

for the solid.

3. NUMERICAL METHOD

3.1. Domain decomposition

The numerical domain was decomposed into three parts: the outer fluid, the inner fluid, and the solid (obstacle). The configuration of the numerical domain is shown in Figure 1. Region I in Figure 1 corresponds to the solid, whose motion was described by Equation (15). The inner fluid region (Region II) corresponds to the fluid near the solid and deforms with the solid. To capture small-scale structures accurately and calculate the pressure and wall shear stress, the mesh should be fine enough in the vicinity of solid. Van Loon *et al*. [5] used local remeshing near the solid to capture this structure [5]. We suggest that an inner domain that deforms with the valve can capture the small structures near the valve without remeshing.

The outer fluid region (Region III) corresponds to the fluid in the channel. Thus, part of the outer fluid region was overlapped by the other two regions. Boundary conditions at the inlet, outlet, and wall were applied to the outer fluid region to model the flow in the channel. An additional constraint was imposed at the inner fluid boundary to match the fluid velocities and pressures between the inner and outer regions, as explained below.

The fluid and solid are connected on the interface without separating. To be able to capture the arbitrary bending of solid, the inner domain may not keep orthogonality. Thus, we take advantage

DOI: 10.1002/fld

of finite-element methods, by which the cross terms that appear in the finite volume or finite-difference formulations due to the nonorthogonal meshes can be avoided. Moreover, the surface integral along the fluid–solid interface can be cancelled out during the assembly of the stiffness matrix by using the finite-element methods. The advantage of this treatment is that the calculation for the surface force on the fluid–solid interface is not necessary. For these reasons, we solve the inner domain by using a finite-element scheme. Compared with the finite-element methods, finite volume methods represent higher efficiency on the simulation of the fluids, particularly for turbulent fluids. The reason partially arises from the time-derivation terms. By using the finite volume scheme, the time-derivative terms are assembled to the diagonal components of the Jacobian or stiffness matrix. Thus, small time steps efficiently optimize the eigenvalues of matrix and accelerate the convergence. For these reasons, we calculated the outer domain using the finite volume scheme.

3.2. Overset ALE

The coupling between the inner fluid region and the fixed outer fluid region was done implicitly using the ghost points method of Henshaw and Schwendeman [20, 21]. The velocities and pressure in the inner domain were enforced to match with those in the outer domain on the surface γ,

$$\mathbf{v}_{\mathrm{o}} - \mathbf{v}_{\mathrm{i}} = \mathbf{0} \quad \text{and} \quad p_{\mathrm{o}} - p_{\mathrm{i}} = \mathbf{0} \quad \text{when } \mathbf{X} \in \gamma \tag{16}$$

Lagrange interpolating polynomials are utilized to achieve this goal. As shown in Figure 2, the velocities and pressure on the point I_1 are calculated by velocities and pressure on O_1 and O_2. $\mathbf{v}_{I_1}$ is defined by $(L_2\mathbf{v}_{O_1} + L_1\mathbf{v}_{O_1})/(L_1 + L_2)$. In the same way, the values on the points I_6, O_3, and O_4 are calculated by the corresponding matching points in the outer or inner layer.

Meanwhile, since the inner mesh deforms with the valve, the arbitrary ALE method was used to account for the effect of the moving mesh on the momentum equations. The conservation of momentum for the inner fluid was written as

$$\frac{\partial \mathbf{v}}{\partial t} + (\mathbf{v} - \mathbf{v}_{\mathrm{mesh}}) \cdot \nabla \mathbf{v} + \nabla p - \frac{1}{Re} \nabla \cdot (\nabla \mathbf{v} + \nabla \mathbf{v}^{\mathrm{T}}) = \mathbf{0} \tag{17}$$

where $\mathbf{v}_{\mathrm{mesh}}$ is the velocity of the inner mesh. The additional term $\mathbf{v}_{\mathrm{mesh}}$ accounts for the changes of the momentum flux at a mesh point due to the motion of the inner grid. The only constraint on

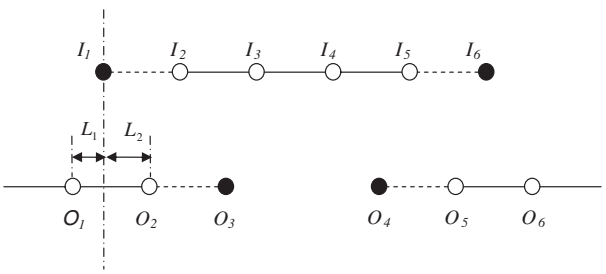

Figure 2. Configuration of the numerical meshes. The points marked with I or O stand for the inner or outer domains, respectively. The white circles connected by solid line are calculated through the numerical method proposed by this paper. The black circles are ghost points.

DOI: 10.1002/fld

mesh motion was to guarantee that the inner and valve regions attach without overlap or separation. In this study, each node of the inner fluid mesh was assigned the same displacement as the nearest node in the solid mesh.

In summary, the complete set of equations for the three regions is as follows:

Outer fluid:

$$\frac{\partial \mathbf{v}}{\partial t} + \mathbf{v} \cdot \nabla \mathbf{v} + \nabla p - \frac{1}{Re} \nabla \cdot (\nabla \mathbf{v} + \nabla \mathbf{v}^{\mathrm{T}}) = \mathbf{0} \tag{18}$$

$$\nabla \cdot \mathbf{v} = 0 \tag{19}$$

Inner fluid:

$$\frac{\partial \mathbf{v}}{\partial t} + (\mathbf{v} - \mathbf{v}_{\mathrm{mesh}}) \cdot \nabla \mathbf{v} + \nabla p - \frac{1}{Re} \nabla \cdot (\nabla \mathbf{v} + \nabla \mathbf{v}^{\mathrm{T}}) = \mathbf{0} \tag{20}$$

$$\nabla \cdot \mathbf{v} = 0 \tag{21}$$

Solid valve:

$$\frac{\mathrm{D}^2 \mathbf{x}}{\mathrm{D}t^2} - \tilde{E} \nabla \cdot \left[\mathbf{B} - \frac{\ln(\det \mathbf{B})}{1 - 2v} \mathbf{I} \right] = \mathbf{0} \tag{22}$$

Inner–outer velocity matching:

$$\mathbf{v}_{\mathrm{o}} - \mathbf{v}_{\mathrm{i}} = \mathbf{0} \quad \text{and} \quad p_{\mathrm{o}} - p_{\mathrm{i}} = \mathbf{0} \tag{23}$$

When $\det \mathbf{B}$ is close to 1, we approximate $\ln(\det \mathbf{B})/(2v - 1)$ by $(\det \mathbf{B} - 1)/(2v - 1)$.

The unknowns were the inner and outer fluid velocities and pressures, and the displacements and isotropic stress in the solid valve. At the solid–inner fluid boundary, the no-slip boundary condition was enforced strongly.

3.3. Numerical strategy

The equations governing the inner fluid and the solid were solved using the standard Galerkin finite-element method with piecewise biquadratic basis functions for the fluid velocity and solid displacements, and discontinuous piecewise bilinear basis functions for pressure in the liquid and isotropic stress in the solid. The resulting matrix problem at each Newton iteration step was solved using GMRES with ILUT preconditioning [22].

The outer fluid was solved using the finite volume method. In the form of finite volume scheme, the Navier–Stokes equation is

$$\frac{\delta \mathbf{v}}{\delta t} + \int_{\partial V} (\mathbf{n} \cdot \mathbf{v}) \mathbf{v} + \int_{\partial V} p \mathbf{n} - \frac{1}{Re} \int_{\partial V} \mathbf{n} \cdot (\nabla \mathbf{v} + \nabla \mathbf{v}^{\mathrm{T}}) \, \mathrm{d}v + \lambda = \mathbf{0} \tag{24}$$

$$\int_{\partial V} \mathbf{n} \cdot \mathbf{v} = 0 \tag{25}$$

where V is the volume, ∂V is the boundary of volume V, and $\mathbf{n}$ is the normal direction of the surface of ∂V. The second-order backward Euler scheme was utilized for time-derivative

DOI: 10.1002/fld

discretization,

$$\frac{\delta \mathbf{v}}{\delta t} \approx \frac{3\mathbf{v}_k - 4\mathbf{v}_{k-1} + \mathbf{v}_{k-2}}{2\Delta t} \tag{26}$$

where $\mathbf{v}_k$ is the velocity at the kth time step, and $\mathbf{v}_{k-1}$ and $\mathbf{v}_{k-2}$ are the velocities at the two preceding time steps, and Δt is the time-step size. The second-order centred difference was used for the spatial-derivative discretization, i.e. the derivative at the ith node along the x direction was approximated as

$$\frac{\delta \mathbf{v}}{\delta x} \approx \frac{\mathbf{v}_{i+1} - \mathbf{v}_{i-1}}{2\Delta x} \tag{27}$$

where $\mathbf{v}_{i-1}$ is the velocity at the previous node and $\mathbf{v}_{i+1}$ is the velocity at the next one. The discretized equations were solved by using a lower–upper symmetric Gauss–Seidel (LU-SGS) scheme [23].

At the each pseudo-time step, the velocities and pressure at the specific point of outer domain covered by the inner domain are updated by the extrapolation of the corresponding data in the inner domain.

3.4. Numerical set-up

A two-dimensional channel with a flexible obstacle was simulated. The height and the length of the channel were taken to be $2L$ and $40L$. The obstacle was placed at the midpoint of the channel along the flow direction, i.e. at a distance of $20L$ from the inlet. The length of the obstacle is L or $1.4L$. The obstacle was modelled as a neo-Hookean solid with Poisson's ratio 0.491. The configuration of the numerical set-up is shown in Figure 1, and the parameters used are listed in Table I.

To investigate the effect of Reynolds number and elastic modulus on the interaction between the valve and the fluid, the governing equations were solved for two sets of conditions. In the first set, the dimensionless elastic modulus was fixed at 631.23 (this number was selected so that the dimensional elastic modulus was 1500 Pa for a fluid with property of water at 20°C) and the Reynolds number was varied from 350 to 550. In the second set, the Reynolds number was fixed at 500 while the dimensionless elastic modulus of valve is varied from 500 to 2000. To examine

Table I. Parameters used to study coupled flow in a two-dimensional channel.

Parameter	Value
Viscosity of fluid	1.002×10^{-3} N s/m^2
Height of valve	0.01 m
Time-step size	$0.01L/U_b$
Density of fluid	1×10^3 kg/m^3
Density of valve	1.2×10^3 kg/m^3
Valve element size, in units of L	0.02×0.04
Inner fluid element size, in units of L	0.02×0.04
Outer fluid mesh discretization size, in units of L	0.1×0.04

DOI: 10.1002/fld

the long-time statistical behaviour of solid and fluid, velocities, pressure, and deformation data were averaged over 6000 numerical steps.

4. RESULTS

The solutions of the governing equations were checked for mesh convergence. Figure 3 shows the velocity profile across the channel at a distance L downstream from the valve for $Re = 500$ and dimensionless elastic modulus $\tilde{E} = 631.23$ for two meshes: one whose element dimension along the flow direction is half of that of the other. The agreement between the two velocity profiles indicates that the solution of the governing equations is independent of the mesh size for the mesh used. The mesh resolution of the results was further examined in Figure 4, in which the distribution of the time-averaged wall shear stress $\mu\partial\mathbf{v}/\partial\mathbf{X}|_{\text{wall}}$ is plotted.

The time-averaged wall shear stresses on the lower and upper walls are shown in Figure 4. The solid lines are fine mesh results and the squares are the coarse mesh results. The discontinuity in the lower-wall curve is due to the presence of the valve. There are two reverse-flow regions downstream of the valve, one attached to the bottom wall of the channel and the solid, and the other attached to the top wall of the channel. As seen in Figure 4, the reverse-flow region, where the wall shear stress on the lower wall is negative, moved downstream with rising Reynolds number. When the dimensionless elastic modulus was lowered, the solid valve deflected more, and the size of reverse-flow region shrank, as seen by comparing the reverse-flow regions in Figures 4(b)–(d).

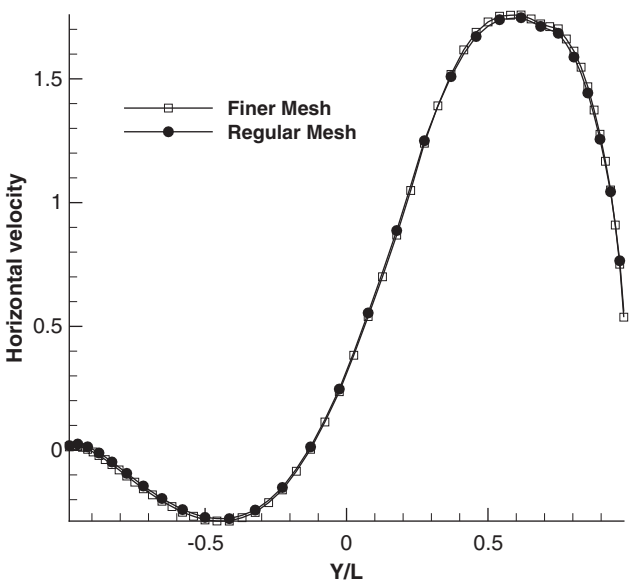

Figure 3. Velocity in the flow direction at a distance L downstream of the valve. Velocity profiles for two different meshes, one whose finite elements and control volumes were half the other's, match indicating that the solutions are independent of the mesh resolution.

DOI: 10.1002/fld

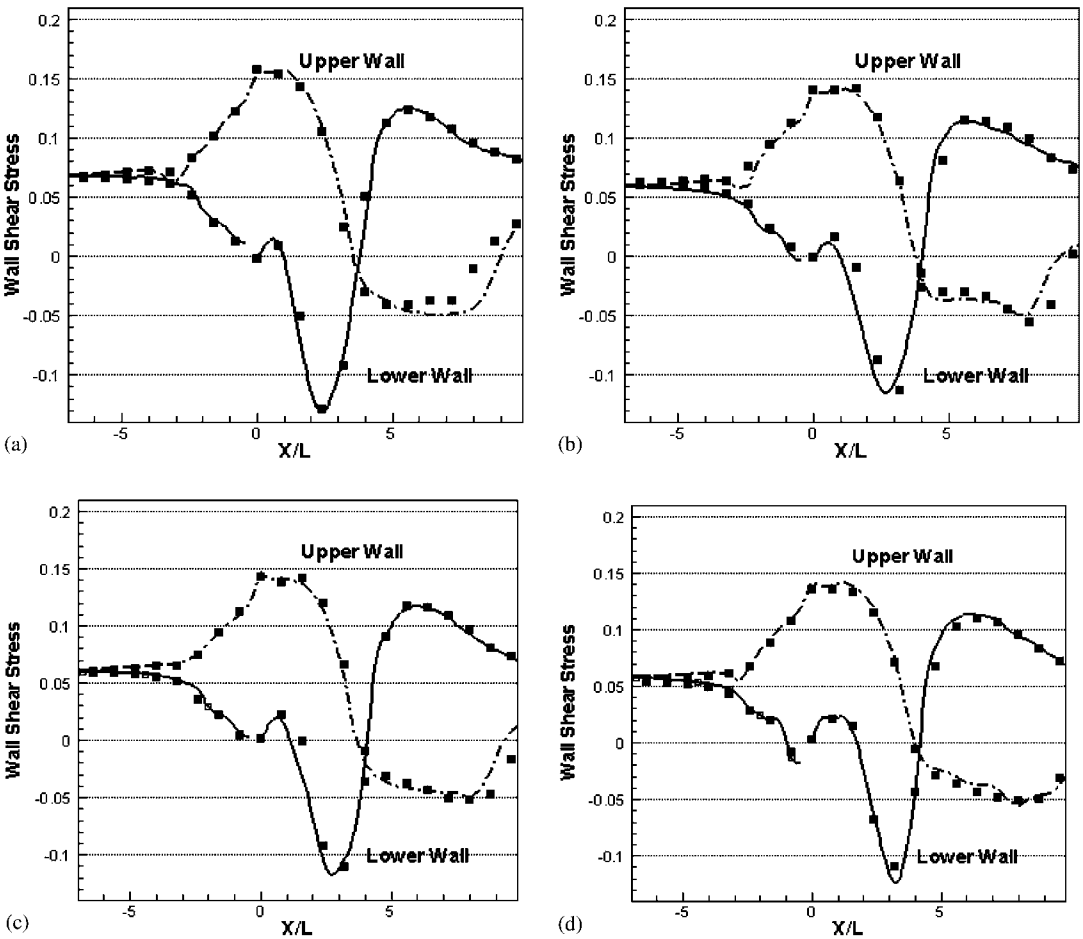

Figure 4. Wall shear stress along the top and bottom walls at different locations along the flow direction. The gap in the bottom curve is due to the presence of the valve. The solid lines are the results from the fine mesh. And the black squares are the results from the coarse mesh: (a) $Re = 400$, $\tilde{E} = 631.23$; (b) $Re = 500$, $\tilde{E} = 631.23$; (c) $Re = 500$, $\tilde{E} = 589.15$; and (d) $Re = 500$, $\tilde{E} = 505$.

Table II. Size of down-stream reverse fluid and the maximum deformation of solid for different Reynolds numbers and dimensionless elastic modulus.

	Case 1	Case 2	Case 3	Case 4	Case 5
Reynolds number	400	500	500	500	500
Dimensionless elastic modulus	631.23	631.23	589.0	505	400
Size of lower reverse flow	$3.2L$	$2.9L$	$2.6L$	$2.5L$	$2.3L$
Size of upper reverse flow	$4.7L$	$5.9L$	$6.05L$	$6.34L$	$8.46L$
Maximum deformation of solid	$0.28L$	$0.21L$	$0.266L$	$0.43L$	$1.08L$
The length of obstacle	L	L	L	L	$1.4L$

DOI: 10.1002/fld

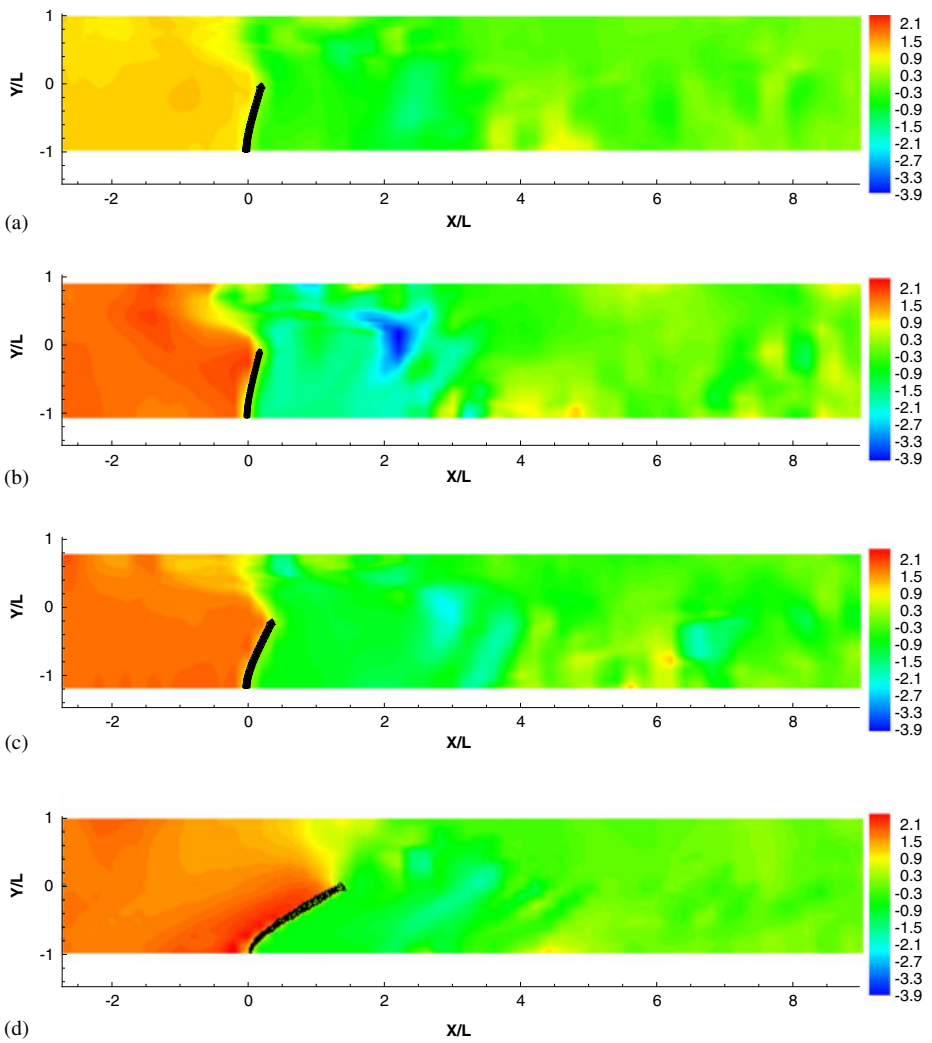

Figure 5. Effect of Reynolds number and dimensionless elastic modulus on pressure distribution: (a) $Re = 400$, $\tilde{E} = 631.23$; (b) $Re = 500$, $\tilde{E} = 631.23$; (c) $Re = 500$, $\tilde{E} = 505$; and (d) $Re = 500$, $\tilde{E} = 400$.

The sizes for the reverse flow on the lower and upper regions of the channel are listed in Table II. Results show that the size of the lower recirculation zone falls whereas that of the upper zone rises when the Reynolds number is raised.

The instantaneous pressure distribution for different Reynolds numbers and dimensionless elastic modulus are shown in Figure 5. The pressure on either side of the valve does not change much for the different conditions. However, a large pressure gradient occurs in the top part of the channel above the valve.

Figure 6 shows the pressure drop *vs* mass flow rate for different Reynolds numbers. The pressure drop shown in Figure 6 is the mean pressure difference between the two sides of the valve. Since

DOI: 10.1002/fld

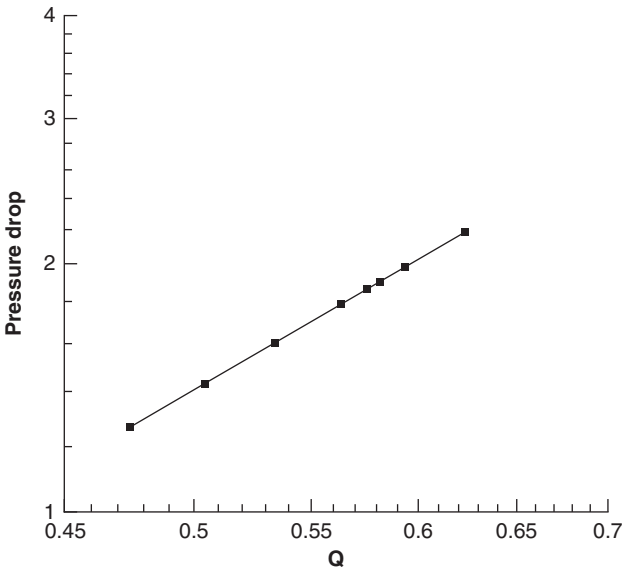

Figure 6. Effect of mass flow rate on pressure drop across the valve. The pressure drop rises with rising mass flow rate.

the mass flow rate is a linear function of the Reynolds number for two-dimensional channel fluid, Figure 6 illustrates the relationship between the dimensional pressure drop and Reynolds number. We plot the dimensional pressure drop with respect to the mass flow rate:

$$\Delta p_{\mathrm{d}} \approx \rho_{\mathrm{F}} U_{\mathrm{b}}^2 = \frac{C}{\rho_{\mathrm{F}} L^2} Q^2 \tag{28}$$

for some constant C. Here, U_{b} is the bulk velocity of the fluid, Q is the mass flow rate for the two-dimensional channel flow, Δp_{d} is the dimensional pressure drop, and $C = \frac{1}{4}$ for the two-dimensional channel fluid in which the height of the channel is $2L$.

The instantaneous horizontal velocity at $t = 100$ is plotted for different Reynolds numbers and elastic moduli in Figure 7. The averaged maximum deformation of the solid is listed in Table II. As expected, both instantaneous field represented by Figure 5 and the averaged data show that lowering the valve modulus causes the valve to deflect more in the flow direction. However, raising the flow rate by increasing the Reynolds number and lowering the valve modulus reduces the deformation of the valve. The dimensionless stress acting on the surface of the valve can be written as

$$\sigma = -p + \frac{1}{Re}(\nabla \mathbf{v} + \nabla \mathbf{v}^{\mathrm{T}}) \tag{29}$$

Since Δp and $\tilde{E}$ both scale as U_{b}^2, the pressure contribution to deflection of the obstacle is unchanged when Re is changed but $\tilde{E}$ is not. The viscous stress contribution from (28), however,

DOI: 10.1002/fld

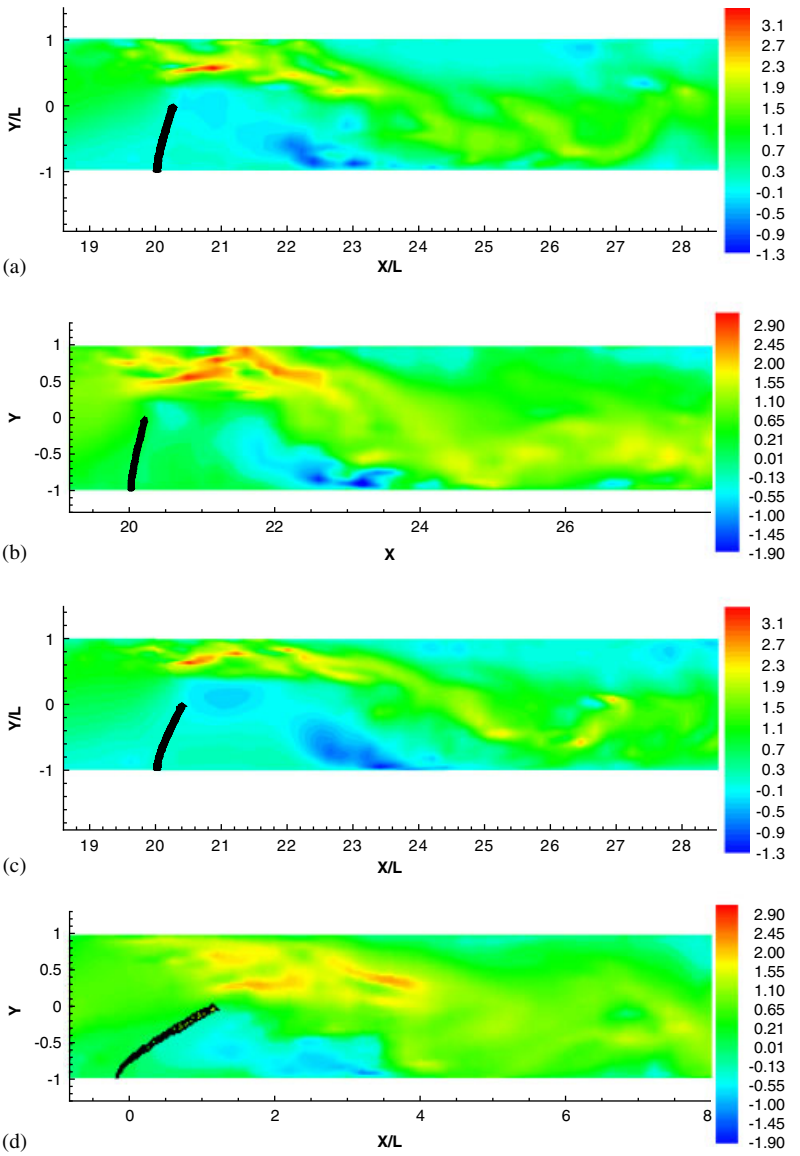

Figure 7. Effect of Reynolds number and dimensionless elastic modulus on the horizontal component of the fluid velocity: (a) $Re = 400$, $\tilde{E} = 631.23$; (b) $Re = 500$, $\tilde{E} = 631.23$; (c) $Re = 500$, $\tilde{E} = 505$; and (d) $Re = 500$, $\tilde{E} = 400$.

scales as U_b. So keeping $\tilde{E}$ constant and increasing Re decreases the viscous stress contribution. Thus, increasing Re and keeping $\tilde{E}$ constant decreases the deflection at the obstacle.

Figure 8 shows the mean horizontal velocity profiles at different locations along the channel. The recirculation zone in the downstream of the solid is clearly evident in the figure.

DOI: 10.1002/fld

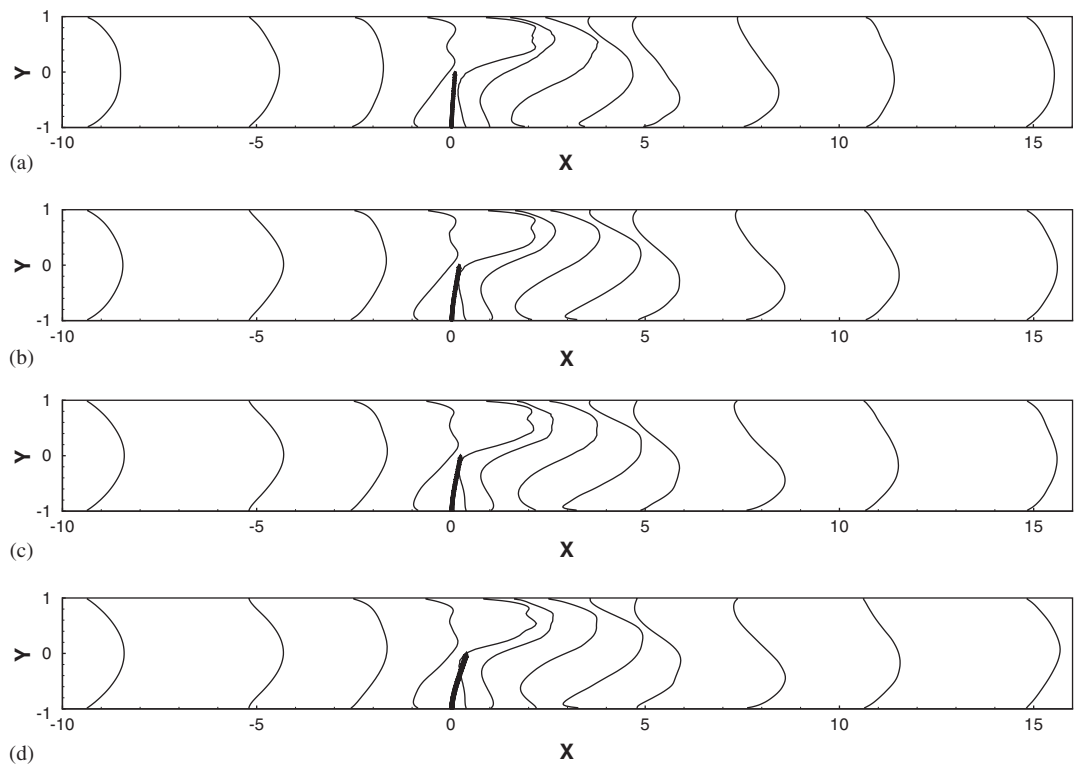

Figure 8. Mean horizontal velocities for different Reynolds number and elastic modulus. The velocity profiles correspond to the locations $-9.5L$, $-5.2L$, $-2.5L$, $-0.6L$, $0.5L$, L, $2.4L$, $3.7L$, $5L$, $7.5L$, $10.5L$, and $15L$ away from the valve: (a) $Re = 400$, $\tilde{E} = 631.23$; (b) $Re = 500$, $\tilde{E} = 631.23$; (c) $Re = 500$, $\tilde{E} = 589.15$; and (d) $Re = 500$, $\tilde{E} = 505$.

5. CONCLUSION

The method presented above achieved its goal—to solve a coupled-flow problem of a two-dimensional channel flow with a thin flexible structure. The major advantage of our method is that no remeshing is necessary to handle the pressure jump due to the solid. This lowers the computational cost, and will allow us to use a structured-grid solver, which although of small significance in the two-dimensional case will be valuable in the three-dimensional case. The presence of the inner mesh makes the pressure and velocity gradients in the outer mesh smooth and facilitates use of the ghost point approach.

Our ultimate goal is to model motion of bio-artificial and native heart valves, with particular emphasis on the aortic valve. The cardiac valve problem is much harder than the test problem posed here, because it involves three-dimensional pulsatile flow and root distension. Also, the mechanical behaviour of the valve is far more subtle than that of a homogeneous neo-Hookean solid, as shown previously by numerous experimental and theoretical studies [5, 6, 13]. Baaijens and co-workers have made considerable progress in incorporating these factors into their models

DOI: 10.1002/fld

[5, 13], and others have examined the mitral valve [6], again accounting for some of the factors described above. The method described herein provides the potential to solve the cardiac valve problem with greater efficiency and accuracy than previous models, but the numerical studies reported here should be taken only as demonstrations of potential, not as a representation of an actual valvular behaviour.

Two issues will be of particular importance in describing heart valve mechanics. First, the heterogeneous, anisotropic, non-linear mechanics of the valve leaflet must be considered. In theory, our method could accommodate any mechanical model of the leaflet, but selection and implementation of the model will not be trivial.

The second critical issue that was ignored in the current study is contact between the coapting valve surfaces. If one restricts a study to steady flow through the open valve as was done here, contact does not occur, but real valves obviously close as well as open. Contact has been addressed in fluid-free studies of valve closure and in other biological systems, but the general issue is far from resolved. Our method will have an additional concern in this context. A natural way to handle multiple valve leaflets is to have multiple inner meshes, which would each communicate only with the outer mesh. When two inner meshes start to overlap, a mechanism to combine them and to allow the two meshes—and particularly the two leaflets—to interact directly with each other is needed. We consider contact to be the major challenge in the implementation of our method for full valve simulation.

The physical quantities associated with the coupled flow were calculated and analysed. These quantities are the pressure drop across the valve, the maximum deformation of the valve, the velocity and pressure distributions in the fluid, and the wall shear stress. As Reynolds number rises, the pressure drop across the valve rises, but the size of the lower reverse-flow region and the maximum deformation of the valve decrease. When the dimensionless elastic modulus is decreased, the size of the lower reverse-flow region and the maximum deformation of the valve rises.

ACKNOWLEDGEMENTS

The assistance of Phil Bransford and Matt Stay are gratefully acknowledged. This work is supported by the National Institutes of Health grant 1R01 HL071538-01. Computations were made possible by a resources grant from the University of Minnesota Supercomputing Institute.

REFERENCES

1. Kamakoti R, Shyy W. Fluid–structure interaction for aeroelastic applications. *Progress in Aerospace Sciences* 2004; **8**:535–558.
2. Heys J, Barocas V, Taravella M. Modelling passive mechanical interaction between aqueous humor and iris. *Journal of Biomechanical Engineering* 2001; **123**(6):540–547.
3. Perktold K, Rappitsch G. Computer simulations of local blood flow and vessel mechanics in a compliant carotid artery bifurcation model. *Journal of Biomechanics* 1995; **28**(7):845–856.
4. Leuprecht A, Perktold K, Prosi M, Berk T, Trubel W, Schim H. Numerical study of hemodynamics and wall mechanics in distal end-to-side anastomoses of bypass grafts. *Journal of Biomechanics* 1995; **35**(2):225–236.
5. Van Loon R, Anderson PD, de Hart J, Baaijens FPT. A combined fictitious domain/adaptive meshing method for fluid–structure interaction in heart valves. *International Journal for Numerical Methods in Fluids* 2004; **46**:533–544.
6. Einstein DR, Kunzelman KS, Reinhall PG, Nicosia MA, Cochran RP. The relationship of normal and abnormal microstructural proliferation to the mitral valve closure sound. *Journal of Biomechanical Engineering* 2005; **127**:134–147.

DOI: 10.1002/fld

7. Yoganathan AP, Woo Y, Sung H. Turbulent shear stress measurements in the vicinity of aortic heart valve prostheses. *Journal of Biomechanics* 1986; **19**:433–442.
8. Ge L, Jones S, Sotiropoulos F, Healy T, Yoganathan A. Numerical simulation of flow in mechanical heart valves: grid resolution and the assumption of flow symmetry. *Journal of Biomechanical Engineering* 2003; **125**(5):709–718.
9. Bellhouse BJ, Talbot L. The fluid mechanics of the aortic valve. *Journal of Fluid Mechanics* 1969; **35**(4):721–735.
10. Grotberg JB, Jensen OE. Biofluid mechanics in flexible tubes. *Annual Review of Fluid Mechanics* 2004; **36**: 121–147.
11. Sackinger PA, Schunk PR, Rao RR. A Newton–Raphson pseudo-solid domain mapping technique for free and moving boundary problems: a finite element implementation. *Journal of Computational Physics* 1996; **125**:83–103.
12. Michopoulos JG, Farhat C, Fish J. Modeling and simulation of multiphysics systems. *Journal of Computing and Information Science in Engineering* 2005; **5**(3):198–213.
13. Baaijens FPT. A fictitious domain/mortar element. *International Journal for Numerical Methods in Fluids* 2001; **35**:743–761.
14. Peskin CS. Flow patterns around heart valves: a digital computer method for solving the equations of motion. *Ph.D. Thesis*, Physiology, Albert Einstein College of Medicine, 1972.
15. Kim D, Chow H. Immersed boundary method for flow around an arbitrarily moving body. *Journal of Computational Physics* 2006; **212**:662–680.
16. Glowinski R, Pan TY, Hesla TI, Joseph DD, Periaux J. A fictitious domain method with distributed Lagrange multipliers for the numerical simulation of particulate flow. *Contemporary Mathematics* 1998; **218**:B 0-8218-0988-1-03006-5.
17. Xing S, Nhan P-T. Distributed Lagrange multiplier/fictitious domain method in the framework of lattice Boltzmann method for fluid–structure interactions. *Journal of Computational Physics* 2005; **206**:81–94.
18. de Hart J, Peters GWM, Schreurs PJG, Baaijens FPT. A three-dimensional computational analysis of fluid–structure interaction in the aortic valve. *Journal of Biomechanics* 2003; **36**(1):103–112.
19. Humphrey JD. *Cardiovascular Solid Mechanics*. Springer: New York, 2006.
20. Henshaw WD, Schwendeman DW. An adaptive numerical method for high-speed reactive flow on overlapping grids. *Journal of Computational Physics* 2003; **191**:420–447.
21. Henshaw WD, Schwendeman DW. Moving overlapping grids with adaptive mesh refinement for high-speed reactive and nonreactive flow. *Journal of Computational Physics* 2006; **216**:744–779.
22. Saad Y. *Iterative Methods for Sparse Linear Systems* (2nd edn). SIAM Press: Philadelphia, PA, 2003.
23. Yoon S, Jameson A. An LU-SGS scheme for the Euler and Navier–Stokes equations. *AIAA paper 87-600*, 1987.

DOI: 10.1002/fld